

Fabrication, characterization, and simulation of a cantilever-based airflow sensor integrated with optical fiber

M. Sadegh Cheri,^{1,2} Hamid Latifi,^{1,2,*} F. Beygi Azar Aghbolagh,¹ O. R. Ranjbar Naeini,¹ Majid Taghavi,¹ and Mohammadamir Ghaderi^{1,3}

¹Laser & Plasma Research Institute, Shahid Beheshti University, Evin, Tehran 1983963113, Iran

²Department of Physics, Shahid Beheshti University, Evin, Tehran 1983963113, Iran

³Present address: Delft University of Technology, Faculty of EEMCS, Department of ME/EI, Mekelweg 4, Delft 2628 CD, The Netherlands

*Corresponding author: latifi@sbu.ac.ir

Received 23 January 2013; revised 8 April 2013; accepted 13 April 2013;
posted 15 April 2013 (Doc. ID 183941); published 10 May 2013

In this paper, we present the fabrication and packaging of a cantilever-based airflow sensor integrated with optical fiber. The sensor consists of a micro Fabry–Perot (FP) cavity including a fiber and a micro cantilever that is fabricated using the photolithography method. Airflow causes a small deflection of the micro cantilever and changes the cavity length of the FP, which makes the fringe shift. The pressure distribution and velocity streamlines across the cantilever resulted from the airflow in the channel have been simulated by the finite element method. The experimental results demonstrate that the sensor has a linear sensitivity of 190 [fringe shift (pm)] per (l/min) and a minimum detectable airflow change of 0.05 (l/min). © 2013 Optical Society of America

OCIS codes: (060.2310) Fiber optics; (120.0280) Remote sensing and sensors.

<http://dx.doi.org/10.1364/AO.52.003420>

1. Introduction

Measuring gas flow plays an important role in mechanical engineering, environmental monitoring, industrial process control, biotechnology, and chemical and medical applications. Flow sensing by microelectromechanical system (MEMS) technologies, have many advantages compared with their conventional large-scale counterparts, such as anemometers, turbines, Pitot tubes, and so forth [1–7]. MEMS sensors have many advantages including lower power consumption, higher precision, more rapid response, more improved portability, and lower manufacturing cost [8–12].

MEMS-based flow sensors are a good candidate for measuring of gas flow due to the mentioned advantages. These sensors are either thermal or nonthermal. In the thermal type, the gas flow rate is determined by measuring the change in the heat transport capability of the sensing medium caused by its interaction with the airflow. However, thermal airflow sensors have some disadvantages, such as slow response, high power consumption, and low signal level, which limit their application. Moreover, one factor that limits the sensitivity of these sensors is the heat loss from the heating element to the substrate [13,14]. Nonthermal or mechanical flow sensors incorporate a moving mechanical force-sensing structure like a cantilever. The airflow causes a displacement in micro cantilever, which induces a corresponding change in the output of

the sensor [5]. Some of the important sensing mechanisms include piezoresistivity, piezoelectricity, variable capacitance, resonance, and optical techniques. These sensors have advantages such as lower power consumption and easier integration with other microscale systems compared to thermal gas flow sensors [14]. Chen *et al.* reported an artificial hair cell sensor for flow sensing with ultrahigh velocity and angular sensitivity [15]. Although these approaches indicate good sensitivity, they require a relatively complex fabrication process [14]. Among detection methods, the optical airflow sensor has been developed to merge with MEMS technology. One of the well-known optical methods is Fabry–Perot interferometry (FPI) [16–21].

FPI sensors offer many advantages such as immunity to electromagnetic interference, high sensitivity, having remote sensing capability, reduction in size and cost, and applicability in harsh environments [20]. Cipullo *et al.* presented the fabrication and simulation of an airflow velocity sensor based on a fiber-optic ferrule-top cantilever. The authors used a femtosecond laser for carving on the fiber-optic ferrule-top in order to fabricate a cantilever and reported a minimum detectable airflow change equal to 0.07 (m/s) [19]. Caldas *et al.* fabricated a fiber optic hot-wire flow meter based on a metallic coated hybrid long period grating/fiber Bragg grating structure with a flow speed resolution of 0.08 (m/s) [16].

In this paper, we present the fabrication and simulation of a cantilever-based (MEMS) airflow sensor, which is integrated with a fiber optic. This sensor has a linear sensitivity change of 190 [fringe shift (pm)] per (l/min) and a minimum detectable airflow change of 0.05 (l/min). Our sensor was fabricated by a micro fabrication process, which is suitable for mass production and in comparison with other similar work [19] does not need a femtosecond laser for carving a cantilever on the fiber tip. The principle of operation and the simulation of the airflow sensor are discussed in Section 2.

Fabrication, packaging process, and experimental setup are explained in Section 3. In Section 4 the experimental results are discussed.

2. Principle of Operation and Simulation Results

A. Principle of FP Operation

A schematic of cantilever-based airflow sensor is shown in Fig. 1. The main part of the sensor is a

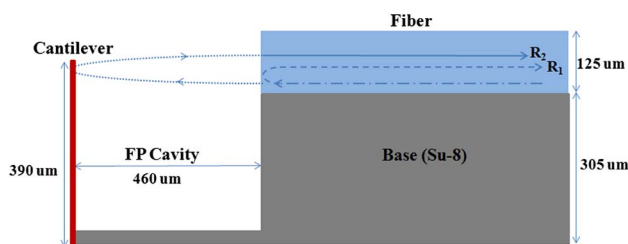


Fig. 1. Schematic view of the airflow sensor.

micro F–P cavity that includes an end cleaved fiber that is placed on the SU-8 base and a vertical micro cantilever. The optical path is shown in Fig. 1. The incident light in the fiber (dashed–dotted line) is first partially reflected (R_1) at the end face of the fiber (dashed line). The rest of the incident light enters the FP’s cavity (dotted line) and is reflected back from the cantilever surface going back to the fiber and then portion of it (R_2), is coupled to the optical fiber (solid line). The interferometric spectrum is observed from the interference of R_1 and R_2 . Reflectance R that has resulted from R_1 and R_2 , can be approximated for low $R_1, R_2 \ll 1$ [22]:

$$R = R_1 + R_2 - 2\sqrt{R_1 R_2} \cos\left(\frac{4\pi nd}{\lambda_0} + 2\phi_0\right), \quad (1)$$

where nd is the optical path, λ_0 is the wavelength of the spectrum and ϕ_0 is the initial phase difference. The value of reflection coefficient R_1 (for interface of air-fiber) is equal to 0.04. The reflection of the cantilever surface was measured experimentally using a power meter to be equal to 0.6. The exiting light from a single-mode fiber (SMF) diverges at a cone angle of 9° – 12° and after being reflected from the cantilever, it reflects back into the SMF with more divergence. Note that only the central portion of the reflected light can be coupled into the optical fiber [23]. Therefore, with increase in length cavity, R_2 coefficient is further reduced. In addition, for large cavity length, the visibility of interferometric spectrum is reduced. We select cavity length $L = 460 \mu\text{m}$ in our design, which is sufficient for considering that the R_2 coefficient is much less than one and also in this length we have a good visibility in the interferometric spectrum. Interferometric maxima occur when an integer number of half-wavelength fits in the FP’s cavity length. Adjacent peak (valley) points in the reflection spectrum can be obtained by:

$$nd = \frac{\lambda_1 \lambda_2}{2(\lambda_1 - \lambda_2)}, \quad (2)$$

where λ_1 and λ_2 ($\lambda_1 > \lambda_2$) are the wavelengths of two adjacent peak (valley) points. The airflow impinges on the cantilever causing a deflection of the cantilever’s tip, which in turn changes the FP’s cavity length resulting in a shift in the FP’s interferometric spectrum.

B. Cantilever Simulation in the Airflow Channel

When the airflow is impinged on the cantilever, drag force causes a bending on the cantilever. In order to investigate the behavior of the cantilever in the airflow channel, a three-dimensional simulation was carried out through the finite element method (FEM). The simulation geometry is a rectangular cube with dimensions of 4 mm width, 4 mm height, and 5 mm length. The mesh is denser on the cantilever, fiber, and base. The simulation region and mesh geometry is shown in Fig. 2. A parametric

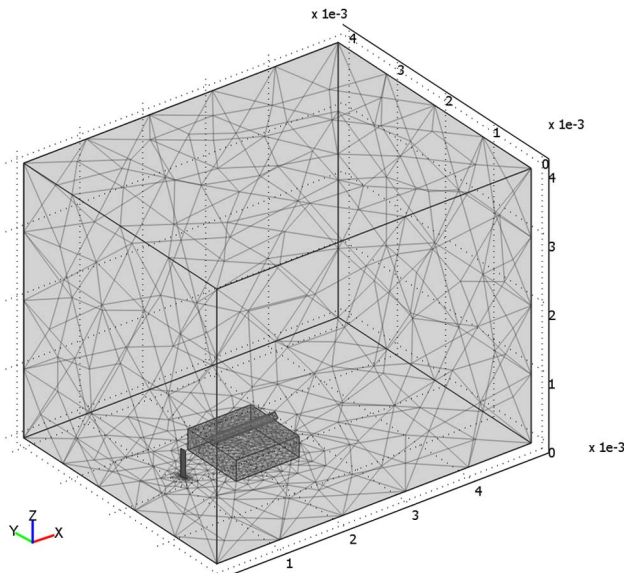


Fig. 2. Simulation region and mesh geometry.

analysis was implemented by changing the input airflow velocity from 0 to 1.19 m/s. These airflow velocities are equal to airflow rates from 0 to 70 (l/h) and the velocity values refer to the centerline ($x = 0, y = 2 \text{ mm}, z = 2 \text{ mm}$). The input airflow is directed toward positive values of the x axis.

The fluid-structure interaction module is used for the fluid dynamics problem in order to obtain pressure distribution and velocity streamlines across two sides of the cantilever in a laminar airflow condition. In this module, the fluid is modeled by incompressible Navier Stokes equation. The cantilever material (copper) has been modeled by using the parameters shown in Table 1.

Figure 3 demonstrates the velocity magnitude distribution in the $x-z$ plane for $y = 2 \text{ mm}$ and 1.19 m/s airflow velocity. As can be seen, the airflow velocity goes to zero on the cantilever borders and the walls the channel, as a consequence of the nonslip boundary.

Figure 4 shows a close view (zoomed view) of the pressure distribution and velocity streamlines across the cantilever inside the channel. As can be seen pressure distribution on the surface of the cantilever especially on the free end of cantilever surface (cantilever's tip) is more than that of the other regions inside the channel. In Fig. 4 scale color from -9.45

Table 1. Parameters for Simulation of Cantilever's Behavior in Airflow Channel (Standard Conditions of 20°C and 1 atm)

Parameters	Value (unit)
Young's modulus	110 (Gpa)
Poisson's ratio	0.35
Dynamic viscosity	1.85×10^{-5} (Pa.s)
Copper density	8700 (kg/m^3)
Air density	1.205 (kg/m^3)

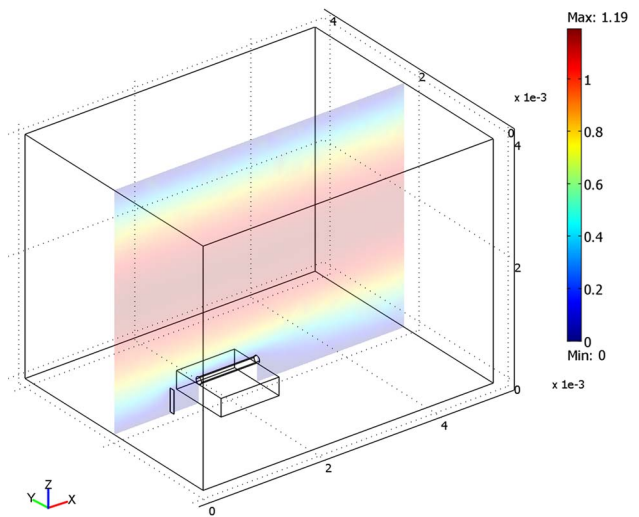


Fig. 3. Velocity magnitude distribution in the $x-z$ plane for $y = 2 \text{ mm}$, calculated for an input airflow centerline velocity of 1.19 m/s.

to 10.64 is selected for illustrating better contrast in the channel.

Figure 5 shows the pressure on the front and back faces of the cantilever at $x = 1 \text{ mm}, y = 2 \text{ mm}, z = 390 \mu\text{m}$, as a function of the input centerline airflow velocity. Both pressures increase quadratically with the input airflow velocity that is expected from Bernoulli's law. The pressure difference between the front and back faces of the cantilever leads to the deflection of the cantilever to positive values of the x axis.

3. Process of Sensor Fabrication

The chip of sensor was fabricated using the photolithography method in three steps and in the final step it is packaged.

A. Fabrication of the Cantilever

At first, SiO_2 substrate was cleaned with 2-propanol, pure acetone and deionized water. Then, a 375 nm thick layer of copper was coated on a cleaned SiO_2 substrate with physical vapor deposition (PVD) method. After that a 7.5 μm thick layer of Ma-P 1275 positive photoresist was spun on it and baked. Reduction

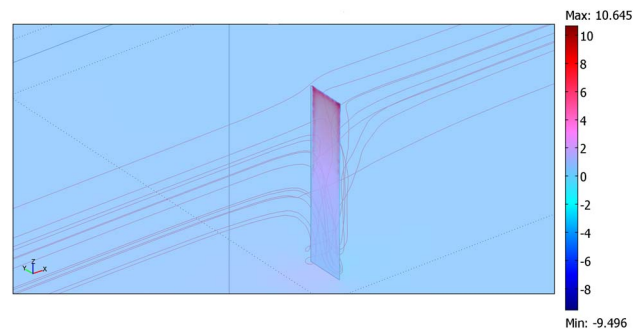


Fig. 4. Pressure distribution (Pa) and velocity streamlines across the cantilever in close view (zoomed view) inside the channel for input airflow centerline velocity of 1.19 m/s.

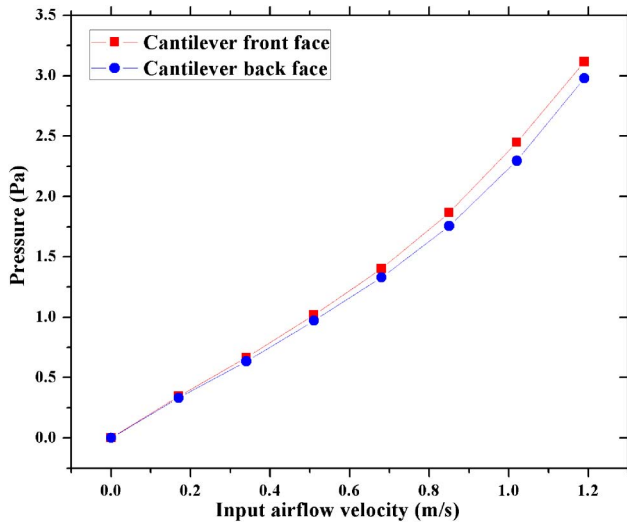


Fig. 5. Pressure on the cantilever front and back surfaces versus input airflow velocity.

projection photolithography setup was used to form the pattern of cantilever with dimensions of $390\ \mu\text{m}$ length and $90\ \mu\text{m}$ width on the photoresist layer. The pattern of cantilever on Ma-P 1275 layer was developed in developer solution and the copper layer was etched in FeCl_3 . The Ma-P 1275 layer was cleaned from the surface of the cantilever with pure acetone. Then the cantilever was separated from

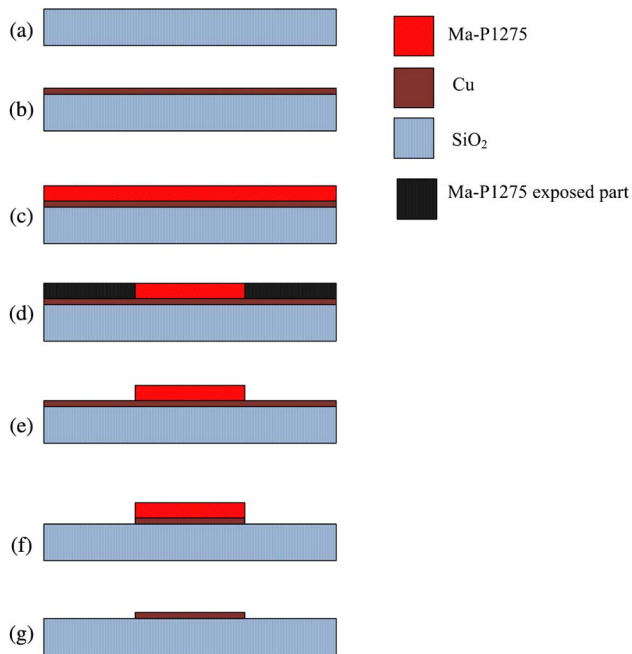


Fig. 6. Fabrication process of the cantilever. (a) SiO_2 substrate was cleaned by 2-propanol, pure acetone, and dionized water. (b) Copper was coated by PVD method. (c) A $7.5\ \mu\text{m}$ thickness Ma-P 1275 was spun coated on copper layer and baked. (d) Photolithography was done for patterning cantilever on Ma-P 1275. (e) Pattern of cantilever on Ma-P 1275 was developed in Ma-P 1275 developer solution. (f) Copper layer was etched in FeCl_3 acid. (g) Ma-P 1275 was cleaned from the surface of the cantilever with pure acetone.

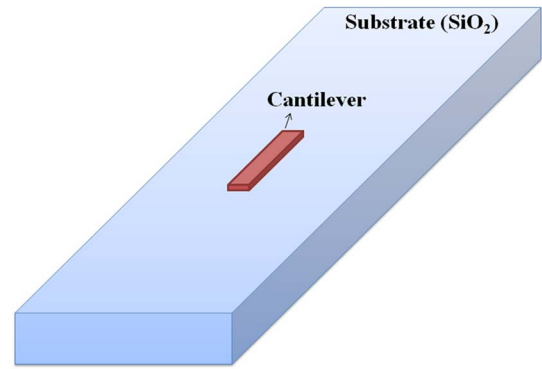


Fig. 7. 3D schematic view of the fabricated cantilever.

the substrate using an ultrasonic bath. Figure 6 demonstrates the fabrication process of the cantilever and Fig. 7 shows a 3D schematic view of the cantilever on the substrate.

B. Fabrication of the Base

For the fabrication of the base, a $25\ \mu\text{m}$ thick layer of SU-8 was spun on a clean SiO_2 substrate and the photolithography was used to form a base with $25\ \mu\text{m}$ height.

Then a $40\ \mu\text{m}$ thick layer of SU-8 was spun and exposed to form another base on the previous layer. We repeated this step for seven times. Therefore, the overall height of the fabricated base was $305\ \mu\text{m}$. The unexposed region was developed in SU-8 developer solution. Figure 8 demonstrates the fabrication process and Fig. 9 shows a 3D schematic view of the fabricated base.

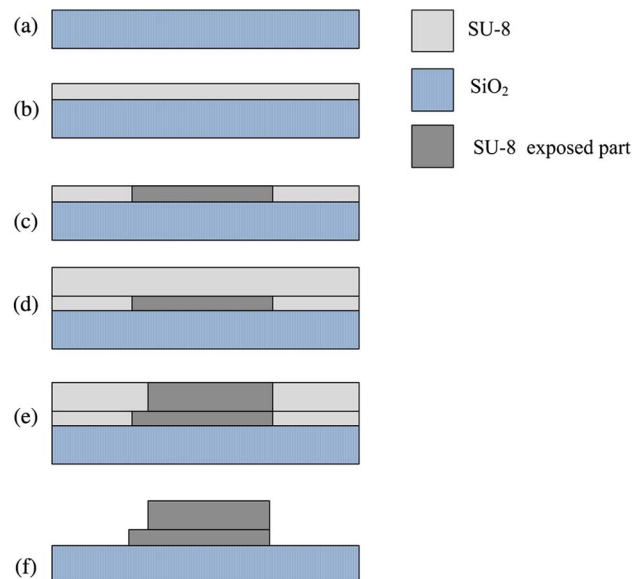


Fig. 8. Fabrication process of the base. (a) SiO_2 substrate was cleaned with 2-propanol, pure acetone, and dionized water. (b) A $25\ \mu\text{m}$ thick layer of SU-8 was spun on SiO_2 substrate. (c) Photolithography was done for patterning of the base. (d) A $40\ \mu\text{m}$ thick layer of SU-8 was spun. (e) Photolithography was done. (f) The unexposed region was developed in SU-8 developer solution [the (d) and (e) steps were repeated seven times].

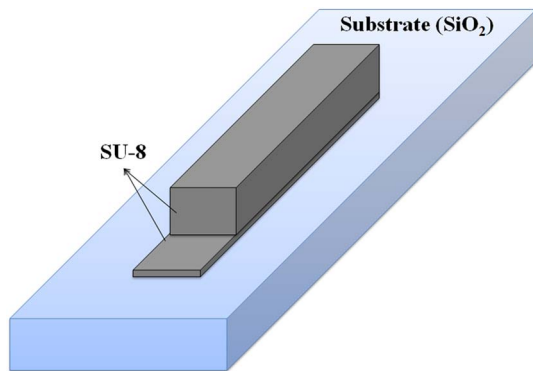


Fig. 9. 3D schematic view of the fabricated base.

C. Connecting the Cantilever Vertically to the Substrate

After releasing the cantilever from the substrate, it was brought close to the base by the use of tweezers and a microscope and then it was secured with glue to the base vertically. Figure 10 shows a 3D schematic view of the cantilever that is connected to the base. Finally, we used tweezers and a microscope to place a single mode end cleaved fiber tip (SMF-28) on the SU-8 base. The fiber was brought close to the micro cantilever's tip and was secured to the SU-8 base with glue. In the process of connecting the cantilever to the base, we tried to glue the cantilever parallel with the fiber surface. The tilt of the cantilever surface at a constant length cavity reduces reflection coefficient R_2 and therefore reduces the visibility of interferometric spectrum. To make sure that the surface of cantilever is parallel with the end of the fiber we observed the interferometric spectrum [Fig. 14(a)] and when we had a maximum visibility we made sure that the cantilever was parallel with the fiber optic.

Even if there is a small tilt angle between the cantilever and fiber surface, it will not affect the final results because it is present on all airflow rates. Figure 11 demonstrates a top view photograph of the fabricated sensor chip, which is taken by microscope and CCD.

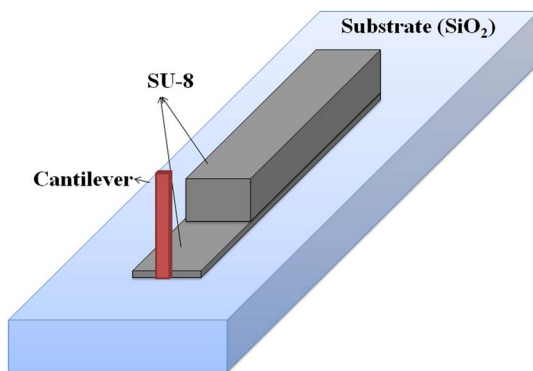


Fig. 10. 3D schematic view of the cantilever connected to the base.

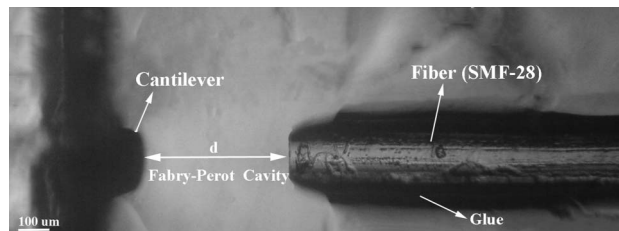


Fig. 11. Top view photograph of the fabricated sensor chip.

D. Final Packaging of the Airflow Sensor

In the final step, two slabs of Poly(methyl methacrylate) (Plexiglas) with the thickness of 5 and 3 mm, and the length and width of 8.5 and 3.5 cm, respectively, were used for the final packaging of the airflow sensor. In the first step, with the use of a 35 W CO₂ laser, a channel with 4 mm width, 4 mm depth, and 8.5 cm length was ablated on the Plexiglas. In the second step, a flat rectangular pit with the thickness of 1 mm and the length and width of 7.62 and 2.54 cm, respectively, and one slit for placing the fiber with 150 μm width and depth and 50 mm length were ablated on the Plexiglas by CO₂ laser. Then the sensor chip in Fig. 11 was placed on the flat rectangular pit and glued to the Plexiglas to ensure good seals and mechanical integrity. In the final step, the Plexiglas was aligned on the second Plexiglas and a flexible tube was placed in the input channel and then sealed together with glue. Figure 12(a) shows the schematic dimensions of the channel and flat rectangular pit. Figure 12(b) shows the fabricated rectangular channel and flat rectangular pit. Figure 12(c) illustrates the final packaging of the sensor. The input airflow passes through a flexible tube to the channel of the sensor and the data are gathered by a fiber.

E. Experimental Setup

The experimental setup is demonstrated in Fig. 13. The airflow, supported by a pressurized gas tank, passes through a flow meter with liter/hour (l/h) resolution. Then, the airflow passes through a tube with 4 mm inside the diameter, enters the channel of the sensor and deflects the cantilever's tip. The SM fiber (SMF-28), which was placed in 460 μm away from the micro cantilever, was connected to a superluminescent diode (SLD) by the use of a circulator and an isolator. The light reflected from the fiber, in order to be analyzed, is sent to an optical spectrum analyzer (OSA) by a circulator.

4. Results and Discussion

Figure 14(a) shows the Gaussian shape of SLD spectrum, which is modulated by interference pattern characteristic of a F-P cavity in the range of 1520–1590 nm at 10 (l/h) input airflow rate. By using Eq. (2) and selecting two adjacent peak points, the initial cavity length equal to 460 μm is obtained. The pressure of the input airflow bends the free end of the micro cantilever. By changing the airflow rates from 10 to 70 (l/h), the cavity length varies and the

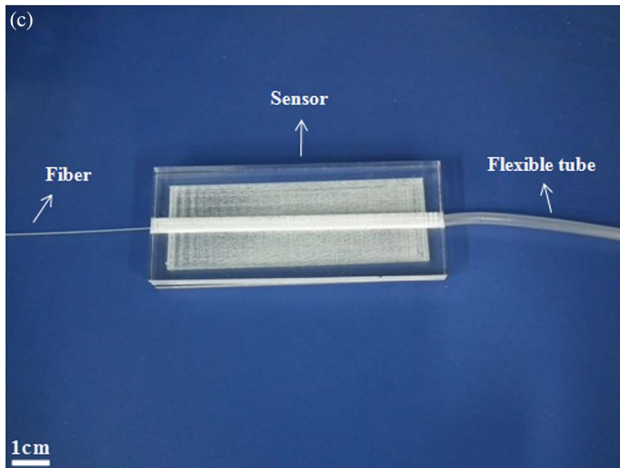
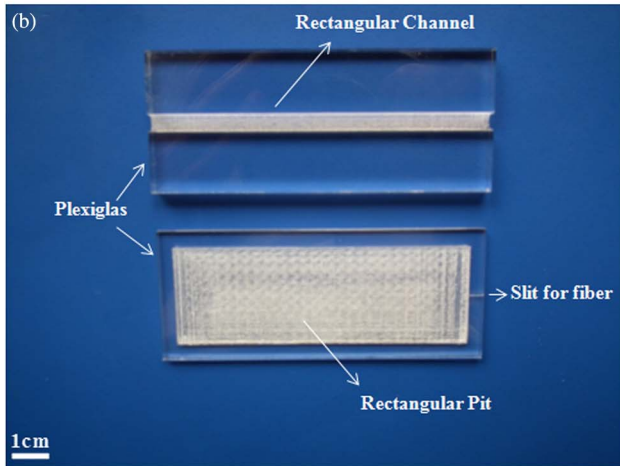
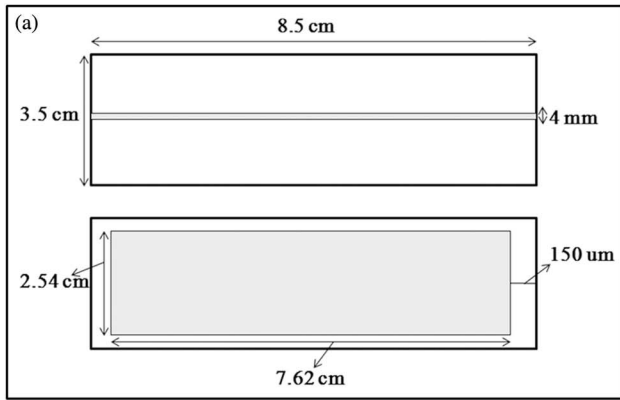


Fig. 12. (a) Schematic photo from the dimensions of the channel and flat rectangular pit (shadow zones should be ablated by laser). (b) A photograph of the channel and flat rectangular pit fabricated by CO₂ laser on the Plexiglas. (c) A photograph of the final packaged sensor.

fringes shift. Figure 14(b) displays the shift of fringes for the input airflow rates from 10 to 70 (l/h) and for one test. The linear relation between the input airflow rates and the shift of fringe is shown in Fig. 15. The shift of fringe is calculated by subtracting the initial wavelength at zero airflow from wavelengths at airflow rates of 10, 20, 30, 40, 50, 60, and 70 (l/h). It has a linear relationship with $R^2 = 0.97$ regression coefficient.

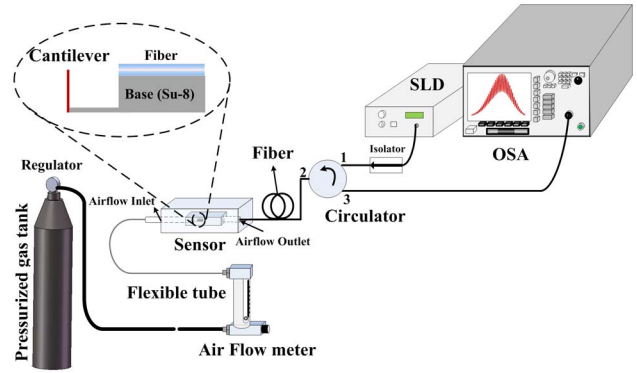


Fig. 13. Schematic view of the experimental setup.

According to Fig. 15, the sensitivity of the airflow sensor is obtained from the slope of the graph, which is equal to 190 [fringe shift (pm)] per (l/min). In Fig. 15, each point is an average of four tests. The minimum detectable airflow change is calculated using the spectral resolution of the OSA (10 pm) to be 0.05 (l/min). According to the cross section of the channel in our sensor (4 mm × 4 mm) this resolution is equal to the minimum detectable airflow change 0.05 (m/s).

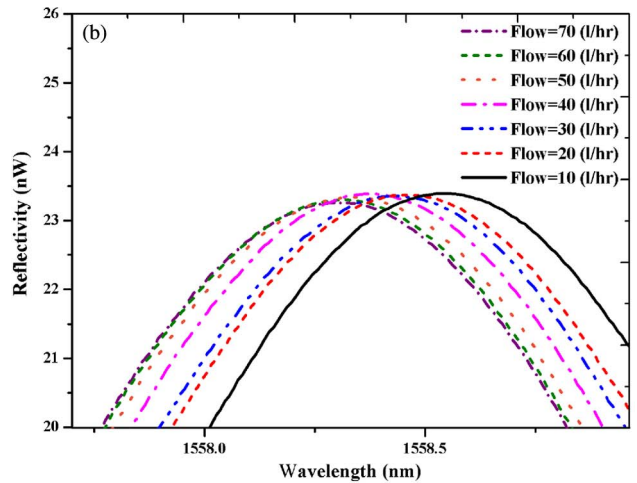
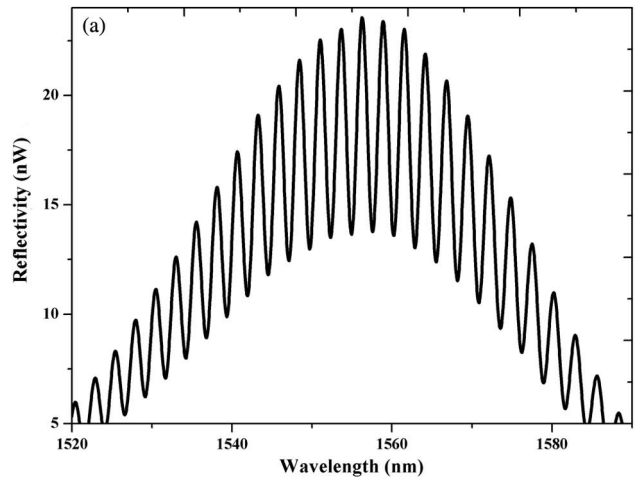


Fig. 14. (a) Interferometric fringes at 10 (l/h) input airflow rate. (b) Shift of interferometric fringes for one peak at input airflow rates of 10, 20, 30, 40, 50, 60, and 70 (l/h).

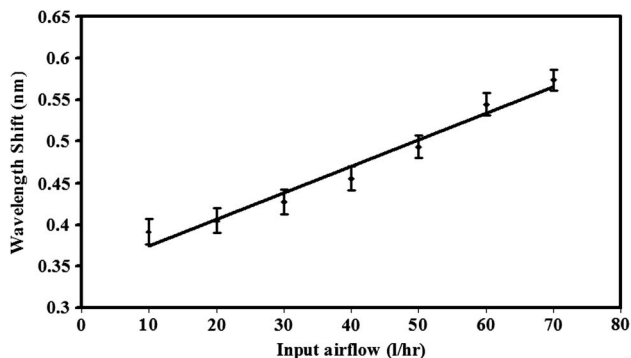


Fig. 15. Linear relation between the airflow rate and fringe shift.

This minimum detectable airflow change is slightly better than [16] and [19] that are 0.08 (m/s) and 0.07 (m/s), respectively. It is comparable with commercial anemometers. The experimental deflection (x -displacement) of the initial position of the cantilever's tip versus the input airflow is shown in Fig. 16. The experimental deflection is calculated by subtracting the cavity length for each input airflow rate from the initial cavity length (input airflow rate of zero) and by averaging the four tests. The quadratic behavior of the cantilever deflection versus the input airflow rate conforms to the Bernoulli's law according to the Fig. 5. We have observed that cantilever-based airflow sensor can be affected by long-term drift (5% in roughly 12 h) which is caused by (1) temperature changes in the environment and (2) permanent deformation of the cantilever after a long time of use. A possible solution would be coating the cantilever with a flexible layer such as, PDMS (Polydimethylsiloxane), or using a drift reduction scheme [24].

The humidity in the airflow gradually leads to the oxidation of the cantilever surface and therefore, decreases the reflection coefficient of R_2 and the visibility of the interferometric spectrum. In addition, the temperature (also humidity) changes of airflow

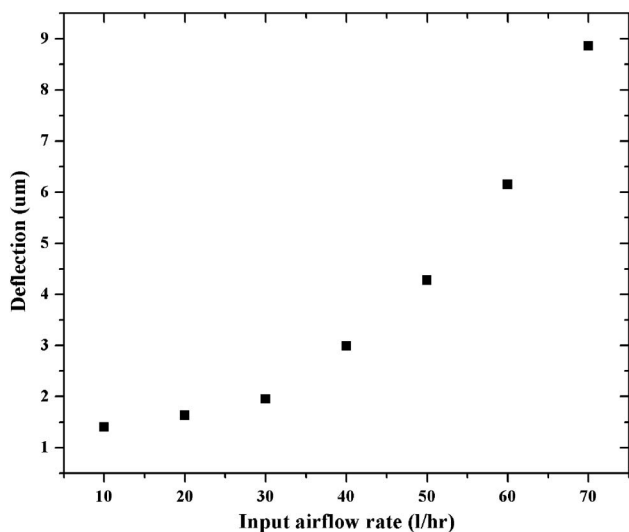


Fig. 16. Experimental results for the deflection of cantilever's tip versus input airflow rate.

results in very slight changes of refractive index (order of magnitude 10^{-7} – 10^{-6}) [25,26], which according to the Eq. (1) leads to the very small shift in interferometric spectrum [Fig. 14(a)].

The use of a laser diode and a data acquisition (DAQ) card as light source and gathering data device instead of an SLD and OSA helps to have a more portable sensor.

So, the sensor has the potential to be used in mechanical engineering environmental monitoring, and industrial process control.

5. Conclusion

In this paper, a cantilever-based airflow sensor is proposed. The process of fabrication, characterization, and simulation for measuring the airflow based on F–P interferometer is implemented. The pressure distribution and velocity streamlines across the cantilever resulted from the airflow in the channel have been simulated by the FEM. In addition, the experimental deflection of the cantilever's tip demonstrates a quadratic behavior versus the input airflow due to Bernoulli's law. The experimental results show that the sensor has a good linear sensitivity of 190 [fringe shift (pm)] per (l/min) and a minimum detectable airflow change of 0.05 (l/min) equal to 0.05 m/s that is comparable with commercial anemometers.

The authors gratefully acknowledge the financial support provided to this study by the Microelectronic Technology Development Council, Iran (micro.isti.ir).

References

1. Y. Xu, C. W. Chiu, F. Jiang, Q. Lin, and Y. C. Tai, "A MEMS multi-sensor chip for gas flow sensing," *Sens. Actuators A* **121**, 253–261 (2005).
2. S. Kim, T. Nam, and S. Park, "Measurement of flow direction and velocity using a micromachined flow sensor," *Sens. Actuators A* **114**, 312–318 (2004).
3. M. Piotta, G. Pennelli, and P. Bruschi, "Fabrication and characterization of a directional anemometer based on a single chip MEMS flow sensor," *Microelectron. Eng.* **88**, 2214–2217 (2011).
4. M. Shikida, T. Yokota, S. Uki, and K. Sato, "Fabrication of monolithically integrated flow sensor on tube," *Sens. Actuators A* **163**, 61–67 (2010).
5. Y. H. Wang, C. Y. Lee, and C. M. Chiang, "A MEMS-based air flow sensor with a free-standing microcantilever structure," *Sensors* **7**, 2389–2401 (2007).
6. R. H. Ma, P. C. Chou, Y. H. Wang, T. H. Hsueh, L. M. Fu, and C. Y. Lee, "A microcantilever-based gas flow sensor for flow rate and direction detection," *Microsys. Technol.* **15**, 1201–1205 (2009).
7. N. J. Allen, D. Wood, M. C. Rosamond, and D. B. Sims-Williams, "Fabrication of an in-plane SU-8 cantilever with integrated strain gauge for wall shear stress measurements in fluid flows," *Procedia Chem.* **1**, 923–926 (2009).
8. Y. Matsuoka, Y. Yamamoto, M. Tanabe, S. Shimada, K. Yamada, A. Yasukawa, and H. Matsuzaka, "Low pressure measurement limits for silicon piezoresistive circular diaphragm sensors," *J. Micromech. Microeng.* **5**, 32–35 (1995).
9. R. Raiteri, M. Grattarola, H. J. Butt, and P. Skládal, "Micro-mechanical cantilever-based biosensors," *Sens. Actuators B* **79**, 115–126 (2001).
10. C. Acar and A. M. Shkel, "Experimental evaluation and comparative analysis of commercial variable-capacitance MEMS accelerometers," *J. Micromech. Microeng.* **13**, 634–645 (2003).

11. G. Soundararajan, M. Rouhanizadeh, H. Yu, L. DeMaio, E. S. Kim, and T. K. Hsiai, "MEMS shear stress sensors for micro-circulation," *Sens. Actuators A* **118**, 25–32 (2005).
12. H. Ernst, A. Jachimowicz, and G. A. Urban, "High resolution flow characterization in bio-MEMS," *Sens. Actuators A* **100**, 54–62 (2002).
13. S. C. Roh, Y. M. Choi, and S. Y. Kim, "Sensitivity enhancement of a silicon micro-machined thermal flow sensor," *Sens. Actuators A* **128**, 1–6 (2006).
14. N. T. Nguyen, "Micromachined flow sensors—a review," *Flow Meas. Instrum.* **8**, 7–16 (1997).
15. N. Chen, C. Tucker, J. M. Engel, Y. Yang, S. Pandya, and C. Liu, "Design and characterization of artificial haircell sensor for flow sensing with ultrahigh velocity and angular sensitivity," *J. Microelectromech. Syst.* **16**, 999–1014 (2007).
16. P. Caldas, P. A. S. Jorge, G. Rego, O. Frazao, J. L. Santos, L. A. Ferreira, and F. Araujo, "Fiber optic hot-wire flowmeter based on a metallic coated hybrid long period grating/fiber Bragg grating structure," *Appl. Opt.* **50**, 2738–2743 (2011).
17. S. Park, S. Kim, S. Kim, and Y. Kim, "A flow direction sensor fabricated using MEMS technology and its simple interface circuit," *Sens. Actuators B* **91**, 347–352 (2003).
18. I. Padron, A. T. Fiory, and N. M. Ravindra, "Novel MEMS Fabry–Perot interferometric pressure sensors," *Mater. Sci. Forum* **638–642**, 1009–1014 (2010).
19. A. Cipullo, G. Gruca, K. Heeck, F. De Filippis, D. Iannuzzi, A. Minardo, and L. Zeni, "Numerical study of a ferrule-top cantilever optical fiber sensor for wind-tunnel applications and comparison with experimental results," *Sens. Actuators A* **178**, 17–25 (2012).
20. J. X. Fang, H. F. Taylor, and H. S. Choi, "Fiber-optic Fabry–Perot flow sensor," *Microw. Opt. Technol. Lett.* **18**, 209–211 (1998).
21. M. Durán-Sánchez, G. Beltrán-Pérez, J. Castillo-Mixcóatl, S. Muñoz-Aguirre, and M. Méndez-Otero, "Experimental study of the fiber laser output intensity behavior and its application to a water flow," *Sens. Actuators B* **123**, 816–821 (2007).
22. X. Wang, B. Li, O. L. Russo, H. T. Roman, K. K. Chin, and K. R. Farmer, "Diaphragm design guidelines and an optical pressure sensor based on MEMS technique," *Microelectron. J.* **37**, 50–56 (2006).
23. G. C. Hill, R. Melamud, F. E. Declercq, A. A. Davenport, I. H. Chan, P. G. Hartwell, and B. L. Pruitt, "SU-8 MEMS Fabry–Perot pressure sensor," *Sens. Actuators A* **138**, 52–62 (2007).
24. C. Song, A. R. Aiyar, S. H. Kim, and M. G. Allen, "Exploitation of aeroelastic effects for drift reduction, in an all-polymer air flow sensor," *Sens. Actuators A* **165**, 66–72 (2011).
25. J. C. Owens, "Optical refractive index of air: dependence on pressure, temperature and composition," *Appl. Opt.* **6**, 51–59 (1967).
26. J. A. Stone and J. H. Zimmerman, "Index of Refraction of Air," <http://emtoolbox.nist.gov/Wavelength/Ciddor.asp>.